

# 1 Size-differentiated Export <sup>c1</sup>Flux in Different 2 Dynamical Regimes in the Ocean

3 M. Dever<sup>1</sup>, D. Nicholson<sup>1</sup>, M. M. Omand<sup>2</sup>, and A. Mahadevan<sup>1</sup>

4 <sup>1</sup>Woods Hole Oceanographic Institution, Woods Hole, MA 02543, USA

5 <sup>2</sup>Graduate School of Oceanography, University of Rhode Island, Narragansett, Rhode Island, USA

## 6 Key Points:

- 7 Submesoscale dynamics enhance the contribution of slow-sinking particles to  
POC export, especially for steep particle size-spectrum slopes
- 8 Remineralization processes intensify the role of slow-sinking particles, to the  
point where these particle sometime dominate POC export

---

<sup>c1</sup> *Text added.*

11 **Abstract**

12 Export of Particulate Organic Carbon (POC) is mainly driven by gravitational sinking.  
 13 Thus, traditionally, it is thought that larger, faster-sinking particles make up most of  
 14 the POC export flux. However, this need not be the case <sup>c1</sup>for particles whose sinking  
 15 speeds are comparable to the vertical velocities of a dynamic oceanic flow field <sup>c2</sup>that  
 16 can influence the descent rate of particles. Particles with different settling speeds <sup>c3</sup>that  
 17 can be affected by the flow are released in two process-oriented model simulations of an  
 18 upper ocean eddying flow <sup>c4</sup>in the Northeast Pacific near Station Papa to evaluate the  
 19 impact of (1) ocean dynamics on the respective contribution of the different sinking-  
 20 velocity classes to POC export, and (2) the particle number size-spectrum slope. The  
 21 analysis reveals that the leading export mechanism changes from gravitationally-driven  
 22 to advectively-driven as submesoscale dynamics become more <sup>c5</sup>active in the region.  
 23 The vertical velocity associated with submesoscale dynamics enhances the contribution  
 24 of slower-sinking particles to POC export <sup>c6</sup>by a factor ranging from 3 to 10, espe-  
 25 cially where the relative abundance of small particles is large, as represented by a  
 26 steep particle size-spectrum slope. <sup>c7</sup>Remineralization <sup>c8</sup> generally decreases the total  
 27 amount of biomass exported, but its impact is weaker in dynamical regimes where  
 28 submesoscale dynamics are present and export is advectively-driven. <sup>c9</sup>In an advec-  
 29 tively-driven export regime, remineralization processes counter-intuitively enhance the  
 30 role of slower-sinking particles to the point where these slower-sinking velocity classes  
 31 dominate the export, therefore challenging the traditional paradigm for POC export.  
 32 This study demonstrates that slow-sinking particles can be a significant contribution,  
 33 and at times, even dominate the export flux.

34 **1 Introduction**

35 Photosynthesis in the sunlit upper ocean and the production of Particulate Or-  
 36 ganic Carbon (POC) takes up dissolved inorganic carbon and facilitates the uptake  
 37 of CO<sub>2</sub> from the atmosphere. The sinking of POC exports organic carbon from the  
 38 upper ocean to the interior, leading to the sequestration of carbon (Falkowski, Barber,  
 39 & Smetacek, 1998) on timescales ranging from days to years depending on the sinking  
 40 depth and circulation. <sup>c10</sup>Despite progress on sampling and viewing particles in the  
 41 ocean, direct measurements of particles sinking velocities are difficult to obtain, and  
 42 often inferred from key parameters such as particle type, size, and density (McDonnell  
 43 & Buesseler, 2012; McDonnell & Buesseler, 2010).

44 Traditionally, POC export is thought to occur through gravitational sinking and  
 45 one-dimensional models have been used to describe the sinking POC flux with depth  
 46 (Armstrong, Lee, Hedges, Honjo, & Wakeham, 2001; DeVries, Liang, & Deutsch, 2014;  
 47 Jackson et al., 1997; Omand, Govindarajan, He, & Mahadevan, 2020). Particles pro-  
 48 duced through primary and secondary production in the surface layer that are rela-  
 49 tively large and fast sinking tend to sink out of the upper surface layer on timescales

---

<sup>c1</sup> in a dynamic oceanic flow field,

<sup>c2</sup> where the ocean velocity

<sup>c3</sup>

<sup>c4</sup>

<sup>c5</sup> important

<sup>c6</sup> A steeper particle size spectrum, also increases the relative contribution of smaller, slower sinking particles

<sup>c7</sup> Implementing a

<sup>c8</sup> scheme

<sup>c9</sup> Under specific conditions

<sup>c10</sup> Text added.

shorter than the timescale on which the particles get remineralized. It is reasonable to treat POC export as sinking-dominated if the vertical advective velocities in the ocean are weaker than the velocities associated with gravitational sinking. However, Particulate Organic Matter (POM) has a wide range of particle shape, size and type, that result in particle sinking velocities ranging from practically zero, to several hundreds of meters per day (Baker et al., 2017; Riley et al., 2012). The size spectrum, or number distribution of particle sizes, is usually characterized by a power law with the power ranging between -2 and -4, for which the abundance of small particles is  $\mathcal{O}(10^4 - 10^8)$  greater than large particles (McCave, 1984; Petrik, Jackson, & Checkley, 2013). The biomass size spectrum, which indicates the distribution of biomass vs. particle size, tends to be flatter and variable in shape (Sheldon, Prakash, & Sutcliffe, 1972) compared to the particle number spectrum, because the volume (and mass) of a particle scales with its linear size raised to a power that exceeds 1 (and typically varies between 2 and 3 depending on shape and porosity). Importantly, it means that a significant fraction of the particulate biomass is in the small size fraction (Richardson & Jackson, 2007). Even though the sinking velocity  $w_s$  of particles does not perfectly relate to particle size  $l$ , it is fair to assume that  $w_s \sim l^n$  (with  $n = 2$  according to Stokes law, and  $1 < n < 2$  for complex particle shapes). Due to this, as well as the fact that particles of organic matter are not very much greater in their densities than seawater, a significant fraction of the biomass sinks very slowly (at velocities less than tens of meters per day). When the gravitational sinking velocity of particles is comparable to (or smaller than) the vertical velocities in the flow field, the dynamics of the flow field can impact the trajectories and fate of the POC. Thus, depending on the flow dynamics, and the fraction of slow-sinking particulate biomass, the sinking of organic matter can be affected by the fluid flow in the ocean.

Recent studies have shown that ocean dynamics can play a role in driving the transport of carbon from the euphotic layer to the ocean interior. For example, enhanced vertical velocities along the edge of a mesoscale eddy led to a funneling of particles along the eddy's periphery (van Haren, Millot, & Taupier-Letage, 2006; Waite et al., 2016) <sup>c1</sup> and in mesoscale features in the California current (Stukel et al., 2017). Omand et al. (2015) found that submesoscale mixed layer eddies, while contributing to the restratification of a frontal zone, were subducting a large amount of non-sinking POC from the surface productive layer during the onset of the Spring bloom in the subpolar North Atlantic. Advectively subducting plumes or filaments of high oxygen, chlorophyll and small POC (evidenced through backscatter) were detected from a suite of gliders during the North Atlantic Bloom experiment (Alkire et al., 2012). Using model simulations to capture the process of eddy-driven subduction, Omand et al. (2015) estimated the downward advective flux of non-sinking POC and parameterized it. Briggs et al. (2011) quantified the flux of fast-sinking particles consisting largely of diatoms from observations of optical backscatter. But, these estimates did not account for a range of sinking particle velocities. Typically, POM has a wide spectrum of sinking velocities and in order to understand its fate and export, we need to consider the biomass distribution as a function of the particle sinking velocity spectrum and its interaction with the dynamics of the flow field in the ocean.

A growing body of literature focusing on submesoscale (1-10 km) dynamics is exploring its impact on biogeochemical processes (Lévy, Ferrari, Franks, Martin, & Rivière, 2012; Mahadevan, 2016). Submesoscale dynamics, characterized by Rossby numbers of order 1, typically develop in filaments in areas where sharp density fronts exist (Klein & Lapeyre, 2009; McWilliams, 2016; Thomas, Taylor, Ferrari, & Joyce, 2013). In this dynamical regime, geostrophic balance breaks down and a secondary ageostrophic circulation develops across the front, capable of generating large vertical

---

<sup>c1</sup> *Text added.*

101 velocities on the order of 100 m/day (Fox-Kemper, Ferrari, & Hallberg, 2008; Mahadevan, 2016). On the denser side of the front, the vorticity is cyclonic and associated  
 102 with downwelling velocities, while anticyclonic vorticity and upwelling is expected on  
 103 the lighter side of the front. The distribution of relative vorticity <sup>c2</sup>associated with  
 104 submesoscale dynamics near the surface exhibits an asymmetry with higher values of  
 105 positive vorticity than negative vorticity (Rudnick, 2001), leading to more localized  
 106 and more intense downwelling regions, as opposed to weaker and larger scale upwelling  
 107 regions (Mahadevan & Tandon, 2006). Enhanced vertical velocities can aid the sup-  
 108 ply nutrients to the sunlit layer of the ocean for primary production (Lévy, Klein, &  
 109 Treguier, 2001; Mahadevan & Archer, 2000) or can significantly increase the export  
 110 of POC to the ocean interior through <sup>c3</sup>localized downwelling (Estapa et al., 2015;  
 111 Gruber et al., 2011; Lévy et al., 2012; Omand et al., 2015).<sup>c4</sup> The downwelling ve-  
 112 locities  $\mathcal{O}(100 \text{ m/day})$  generated at submeso-scales provide a physical mechanism for  
 113 exporting slow sinking or neutrally buoyant particles on timescales shorter than their  
 114 remineralization timescales. If the fraction of biomass associated with such slow sink-  
 115 ing velocities is significant, submesoscale dynamics can potentially impact the export  
 116 of POC.

118 We rely on a submesoscale-resolving, non-hydrostatic ocean model to simulate  
 119 the dynamics in the upper few hundred meters of the ocean. The dynamical model is  
 120 coupled with a particle-tracking module to model the advection of particles by fluid  
 121 flow, while neglecting the effects of particle inertia and drag on their advection. In  
 122 addition, the particles sink with a range of sinking velocities (between 0.025–5 m  
 123 day<sup>-1</sup>) <sup>c1</sup>that is based on the range of vertical currents modeled in this region. We  
 124 aim to address the transitional regime of the particle sinking velocity spectrum, where  
 125 both advection and sinking speeds have similar order of magnitudes. A similar study  
 126 with sinking tracers showed the influence of the flow (Taylor, Smith, & Vreugdenhil,  
 127 2020)<sup>c2</sup>, but the use of particles enables a characterization of export associated with  
 128 each sinking class of particles.

129 The model is used to quantify the contribution of slow-sinking particles to carbon  
 130 export, as a function of (1) the dynamics of the flow field, (2) the slope of the sinking  
 131 velocity spectrum, and (3) the remineralization timescale. Particles in the model  
 132 are prescribed with both a constant and time-varying sinking velocity to mimic a  
 133 remineralizing behavior. Particles are released in two fundamentally different flow  
 134 fields in terms of dynamics based on observed conditions in the Northeast Pacific:  
 135 In the summer, where ocean dynamics are characterized by low Rossby numbers and  
 136 weak vertical advective velocities, and in the winter, where ocean dynamics include  
 137 submesoscale frontal structures and local Rossby numbers  $\mathcal{O}(1)$ . Both simulations  
 138 and the particle-tracking module are described in Section 2. The impact of particles  
 139 characteristics and ocean dynamics on the export of POC is quantified in Section 3,  
 140 and discussed in Section 4. Section 5 summarizes the key conclusions of the study.

## 141 2 Methods

### 142 2.1 Model setup and domain

143 This study uses a non-hydrostatic, three-dimensional, Process Study Ocean Model  
 144 (PSOM; Mahadevan, Olinger, & Street, 1996a, 1996b) to simulate an eddy field that is  
 145 representative of the Northeast Pacific Ocean. The model is set in a channel configura-

<sup>c2</sup> across a front is asymmetric and skewed toward cyclonic vorticity

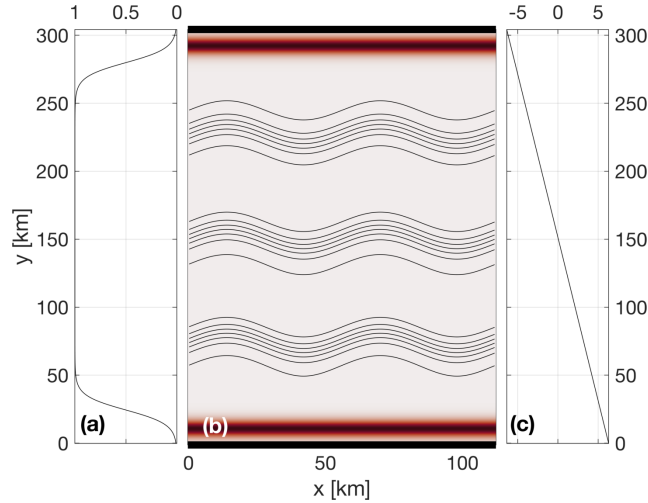
<sup>c3</sup> Text added.

<sup>c4</sup> Text added.

<sup>c1</sup> Text added.

<sup>c2</sup> Text added.

146 tion with periodic east-west boundaries, and solid boundaries in the south and north.  
 147 The domain covers 112 km in the x-direction, 304 km in the y-direction, and 1000 m  
 148 in the vertical (Figure 1). The horizontal resolution is 500 m, while a stretched grid is  
 149 used in the vertical with 32 levels ranging in thickness from 1.25 m near the surface to  
 150 70 m at the lowermost level. The model is integrated numerically in time and evolves  
 151 the temperature, salinity, free-surface height, pressure, and three-dimensional velocity  
 152 field from an initial state, subject to momentum and buoyancy fluxes applied through  
 153 the surface boundary.



154 **Figure 1.** PSOM model setup. (a) Meridional profile of scaling coefficient that multiplies the  
 155 time-varying zonal wind stress  $\tau_x$  shown in Fig. 3a. The taper at north and south boundaries  
 156 prevents ‘coastal’ up-/down-welling being entirely concentrated in the boundary grid cell. (b)  
 157 Restoration factor (color shading) used to dampen internal wave reflection at boundaries as well  
 158 as up-/down-welling due to the windstress curl. Surface density contours (black) show the three  
 159 fronts used to initialize the model. (c) Meridional variation of the time-dependent surface heat  
 160 flux (Fig. 3a) prescribed over the domain.

161 Time-varying wind stress and heat flux are prescribed at the surface boundary.  
 162 Time series are computed from measurements collected at Station Papa and available  
 163 through the Pacific Marine Environmental Laboratory (PMEL, 2018). Daily wind  
 164 stress and net heat fluxes are calculated over the period 2007-2016 to produce a year-  
 165 long climatology. A squared low-pass filter with a cut-off frequency of 8.5 days is  
 166 applied to both time series to remove high-frequency variability. In all numerical  
 167 experiments, simulations are run for the first 5 days without any forcing applied to  
 168 the surface boundary. Surface wind stress and heat fluxes are then linearly ramped up  
 169 between days 5 and 10 of the simulation, to reach realistic values at day 10.

170 While the meridional component,  $\tau_y$ , is set to zero, the zonal component of  
 171 the wind stress,  $\tau_x$ , is prescribed at the surface throughout the model domain and  
 172 is tapered at the northern and southern boundaries to avoid excessive Ekman-driven  
 173 upwelling and downwelling (Figure 1a). A restoration timescale is prescribed to contain  
 174 the curl-driven upwelling and downwelling regions generated by the tapering of the  
 175 wind stress, as well as to limit internal wave reflection at the solid boundaries back  
 176 into the domain (Figure 1b). While net surface heat fluxes are homogeneous in the  
 177 zonal direction, a meridional gradient is maintained throughout the simulation. The

meridional gradient was determined from the North American Regional Reanalysis (NARR) product (Mesinger et al., 2006), and set to  $1/24 \text{ W/m}^2/\text{km}$  (Figure 1c).

Initial hydrographic conditions are determined from a three-dimensional gridded field of temperature and salinity from Argo floats (Gaillard, 2015; Gaillard, Reynaud, Thierry, Kolodziejczyk, & von Schuckmann, 2016). Argo data is averaged monthly over the period 2002-2012 and two different months are used to initialize the two main numerical experiments for this study: Climatological conditions in April are used to initialize the *Papa.summer* experiment, while January climatological conditions are used to initialize the *Papa.winter* experiment (Table 1). The north-south background density gradient is then intensified into three fronts located at  $y = 75$ ,  $y = 150$ , and  $y = 225 \text{ km}$  (Figure 1). The amplitude of the density gradient associated with the three fronts is determined from the probability distribution function (PDF) of the density gradients measured by underwater gliders deployed around Station Papa over the period 2008-2010 (Pelland, 2018; Pelland, Eriksen, & Cronin, 2016). To reduce model spin-up time, density fronts are perturbed by a sinusoidal wave with a wavelength close to the 1st baroclinic deformation radius ( $\lambda = 66 \text{ km}$ ). Similar PSOM configurations were successfully used in previous studies (Mahadevan, D'Asaro, Lee, & Perry, 2012; Omand et al., 2015). <sup>c1</sup>The model does not simulate surface waves or boundary layer turbulence, but rather, examines the fate of particulate organic matter beneath the turbulent surface boundary layer.

Two main experiments are conducted using the same configuration of PSOM, where only initial conditions and surface forcings are varied: *Papa.summer* aims at generating ocean dynamics representing conditions in the Northeast Pacific in the summertime. Summer ocean dynamics are characterized by a flow generally in geostrophic balance, with relatively weak density gradients and low Rossby numbers ( $Ro \ll 1$ ). *Papa.winter* aims at capturing wintertime ocean conditions in the region. A different dynamical regime is expected to dominate during wintertime when mixed layers are deeper and lateral density gradients enhanced, with sharper density fronts, filament-like features and localized Rossby number  $Ro = \mathcal{O}(1)$  over spatial scales  $\mathcal{O}(1 \text{ km})$  (Callies, Ferrari, Klymak, & Gula, 2015; Mensa et al., 2013; Thompson et al., 2016). The individual characteristics of each of *Papa.summer* and *Papa.winter* are detailed below.

### 2.1.1 *Papa.summer* Model Experiment

In *Papa.summer*, PSOM is initialized based on climatological Argo data in April. The magnitude of the density gradient across the front is set to  $3.34 \times 10^{-6} \text{ kg/m}^3/\text{m}$ , which corresponds to the 95<sup>th</sup> percentile of the PDF of density gradients measured in April from glider data collected in the region (Figure 2 and Table 1). The model is run with a timestep of 216 s and is allowed to spin-up for 60 days, allowing summer stratification to develop. The model is then run for 30 additional days, saving instantaneous model fields every 3 hours for particle tracking. The month of April is chosen for initialization so the experiment would capture the onset of positive net heat fluxes, and the summer restratification that ensues in July-August (Figure 2). In this region, the summer stratification is associated with large primary productivity, particle production, and POC export (e.g., fecal pellets, dead phytoplankton; Plant et al., 2016).

---

<sup>c1</sup> *Text added.*

223 **Table 1.** Summary of the key characteristics of PSOM experiments *Papa-summer* and  
 224 *Papa-winter*.

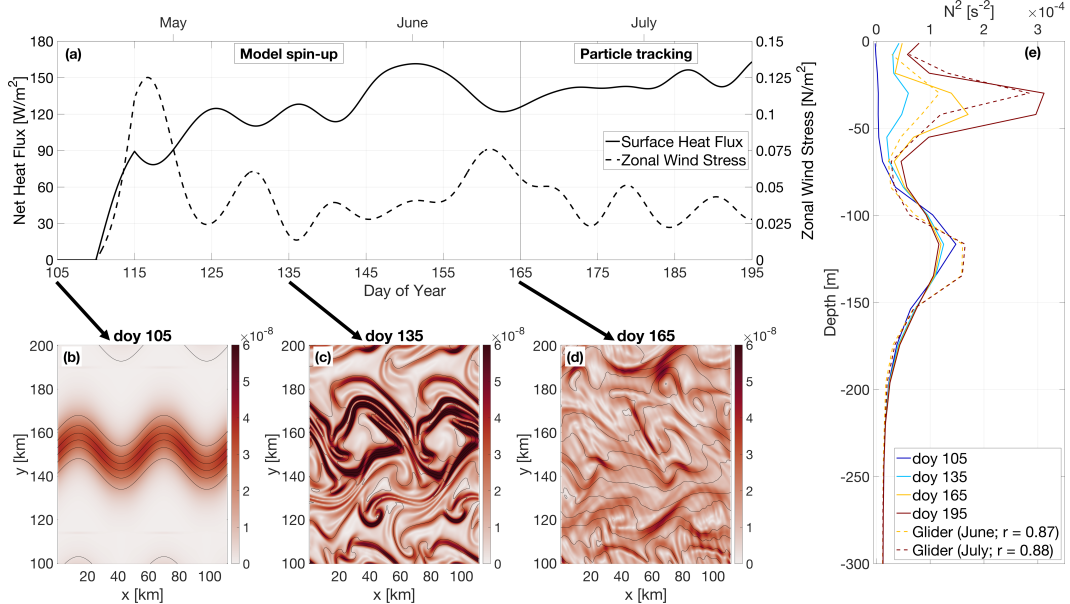
	<i>Papa-summer</i>	<i>Papa-winter</i>
Time period	April – July	January – March
Spin-up	60 days	50 days
Advective timestep	216 s	108 s
Horizontal diffusivity	1 m <sup>2</sup> s <sup>-1</sup>	0.2 m <sup>2</sup> s <sup>-1</sup>
Restoration timescale	3 days	15 days
Zonal wind stress	0 – +0.16 N m <sup>-2</sup>	-0.05 – +0.17 N m <sup>-2</sup>
Surface heat flux	-46.8 – +167.5 W m <sup>-2</sup>	-57.6 – +15.3 W m <sup>-2</sup>
Maximum M <sup>2</sup> ( $\times 10^{-8}$ )		
initial	3.2 s <sup>-2</sup>	33.9 s <sup>-2</sup>
spun-up	12.0 s <sup>-2</sup>	50.0 s <sup>-2</sup>
Maximum N <sup>2</sup> ( $\times 10^{-4}$ )		
initial	1.5 s <sup>-2</sup>	1.6 s <sup>-2</sup>
spun-up	3.1 s <sup>-2</sup>	1.1 s <sup>-2</sup>
Averaged mixed layer depth		
initial	73 m	85 m
spun-up	11 m	93 m

### 2.1.2 *Papa-winter Model Experiment*

235 In *Papa-winter*, PSOM is initialized based on climatological Argo data in January.  
 236 The frontal gradient is set to  $3.54 \times 10^{-5}$  kg/m<sup>3</sup>/m, which corresponds to the  
 237 99<sup>th</sup> percentile of the PDF of density gradients measured in January from glider data  
 238 collected in the region (Figure 3 and Table 1). The model is allowed to spin-up for 50  
 239 days allowing for the prescribed fronts to become unstable. To accommodate for the  
 240 larger density gradients and stronger velocities, the advective timestep is shortened to  
 241 108 s and the horizontal diffusivity is lowered to 0.2 m<sup>2</sup>/s throughout the experiment.  
 242 The model is run for 30 additional days, saving instantaneous model fields every 1.5  
 243 hours for particle tracking. The month of January is chosen for initialization so the  
 244 experiment would capture the time of year where the mixed layer is the deepest, and  
 245 Rossby number O(1) occur more frequently. The objective is for this experiment to  
 246 contrast *Papa-summer* by capturing the statistics of ocean conditions dominated by  
 247 submesoscale dynamics.

### 2.1.3 *Validation*

257 To ensure that PSOM simulations yielded realistic conditions for both *Papa-summer*  
 258 and *Papa-winter*, distributions of horizontal ( $M^2$ ) and vertical ( $N^2$ ) buoyancy gradi-  
 259 ents are compared with glider observations collected over the period 2008-2009 (Pelland  
 260 et al., 2016). During this period, underwater gliders sampled in a “bow-tie” pattern  
 261 centered on Station Papa. Gliders sample the water column in a triangular wave  
 262 pattern, whose shape is easily affected by currents, due to the slow moving speed of  
 263 the glider ( $\sim 1$  km/hr). It is therefore challenging to associate a specific spatial scale  
 264 with gradients computed between glider profiles, as profile separation distances can be  
 265 highly variable through depth and time. To circumvent this issue, horizontal buoy-  
 266 ancy gradients are computed between each pair of glider profiles available within one  
 267 branch of the bow-tie. Each along-track lateral buoyancy gradient is thus associated  
 268 with a specific separation scale and a timestamp. Glider-based density gradients can  
 269 be affected by internal waves. To filter the impact of internal waves on the PDF of



225 **Figure 2.** PSOM configuration for *Papa\_summer*. (a) Time series of net heat fluxes and wind  
 226 stress prescribed at the surface. Notice the positive heat fluxes, as well as downfront winds (i.e.  
 227 eastward) persisting throughout the experiment. (b)-(d) surface horizontal buoyancy gradients  
 228  $M^2 = |\nabla_H b|^2$  (in  $s^{-2}$ ) at day of year (doy) 105, 135, and 165. Black contours show isopycnals (in  
 229 kg/m<sup>3</sup>; CI = 0.01 kg/m<sup>3</sup>). (e) Vertical profile of the buoyancy frequency  $N^2$  at day of year 105,  
 230 135, 165, and 195, showing the development of summer stratification centered at  $z = 30$  m (solid  
 231 lines). Monthly-average vertical stratification obtained from glider profiles collected in June and  
 232 July are superimposed (dashed lines), along with the correlation coefficient between observations  
 233 and model outputs.

270 horizontal buoyancy gradients, only gradients computed at a scale of twice the Rossby  
 271 radius  $\pm 1$  km are considered. Rossby radii are estimated from the glider data and  
 272 are  $\sim 8$  km in winter and  $\sim 20$  km in summer.

## 273 2.2 Particle Tracking Experiments

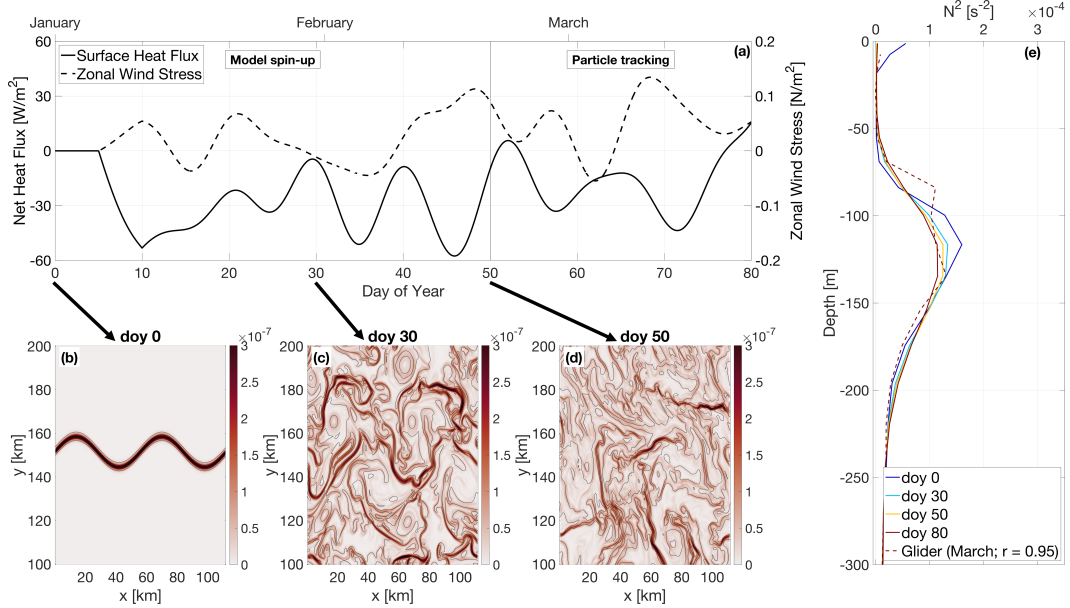
### 274 2.2.1 Particle Advection Scheme

To quantify the impact of submesoscale dynamics on the export of Particulate Organic Matter (POC), Lagrangian particle trajectories are computed using the same scheme as in “TRACMASS” (Döös, Kjellsson, & Jönsson, 2013) with the flow fields from the two experiments described above. The three-dimensional, non-divergent velocity components from the faces of each “C” grid cell are linearly interpolated onto the particle’s position within the grid cell. For example, the eastward (along the x-axis) velocity of a particle is given by

$$u(x) = u_{i-1} + \frac{(x - x_{i-1})}{(x_i - x_{i-1})}(u_i - u_{i-1}), \quad (1)$$

where the subscripts  $i - 1$  and  $i$  denote the western and eastern walls of the grid cell where the particle is located, respectively. This can be re-written as

$$\frac{\partial x}{\partial t} + \beta x + \delta = 0, \quad (2)$$



248 **Figure 3.** PSOM configuration for *Papa\_winter*. (a) time series of net heat fluxes and wind  
 249 stress prescribed at the surface. Notice the mostly negative heat fluxes, as well as alternating  
 250 zonal wind direction. (b)-(d) surface horizontal buoyancy gradients  $M^2 = |\nabla_H b|^2$  (in  $s^{-2}$ ) at day  
 251 of year (doy) 0, 30, and 50. Black contours show isopycnals (in  $kg/m^3$ ; CI = 0.01  $kg/m^3$ ). (e)  
 252 Vertical profile of the buoyancy frequency  $N^2$  at doy 0, 30, 50, and 80, showing the persistence  
 253 of the halocline between  $z = 80$  and  $z = 180$  m throughout the experiment (solid lines). Monthly-  
 254 average vertical stratification obtained from glider profiles collected in March is superimposed  
 255 (dashed line), along with the correlation coefficient between observations and model outputs.

where  $\beta = (u_i - u_{i-1})/\Delta x$  and  $\delta = -u_{i-1} - \beta x_{i-1}$  (Döös et al., 2013). This differential equation can be solved analytically for  $\beta \neq 0$  as

$$x_{t_1} = \left( x_0 + \frac{\delta}{\beta} \right) \exp^{-\beta(t_1 - t_0)} - \frac{\delta}{\beta} \quad (3)$$

The time it will take for the particle to reach the eastern or western face of the grid cell can be computed by taking  $x_{t_1} = x_i$  or  $x_{t_1} = x_{i-1}$ , respectively, and solving for  $t_1$ . For each advective timestep, the times required for the particle to reach any of the 6 walls of the grid cell are computed using (3). If any of those times is shorter than the advective timestep, the particle is advected until it reaches the cell wall. Then the flow field in the adjacent grid cell is considered and the particle is advected over the remaining time.

### 2.2.2 Particle Seeding

For all particle-tracking experiments, a single particle seeding event is prescribed. In the horizontal, particles are seeded every 250 m over the entire domain in the x-direction, and for  $100 < y < 200$  km in the y-direction. The seeding is centered over the mean position of the central front (see Figure 2) and is therefore not affected by undesired effects created by the solid north-south solid boundaries. In the vertical, particles are seeded every 1 m between 75 and 85 m. This depth range is chosen as it corresponds to the average euphotic depth at Station Papa, defined by the 1% light

290 level. <sup>c1</sup>Particle seeding is located at the base of the euphotic layer where biological  
 291 processes not captured by the particles (e.g., grazing, repackaging, aggregation,  
 292 etc.) are not as active (Ducklow, Steinberg, & Buesseler, 2001). The euphotic depth  
 293 was computed for the months of February and June over the period 2007-2016 from  
 294 profiles of Photosynthetically <sup>c2</sup>Active Radiation (PAR) collected at Station Papa as  
 295 part of the long-term monitoring of Line P executed by the Department of Fisheries  
 296 and Ocean Canada<sup>c2</sup>. The average euphotic depth computed for both of these months  
 297 is around 80 m, which agrees with previously established estimates of the euphotic  
 298 depth (Harrison, Whitney, Tsuda, Saito, & Tadokoro, 2004; Sherry, Boyd, Sugimoto,  
 299 & Harrison, 1999).

300 In each particle-tracking experiment, three different classes of particles are re-  
 301 leased. Each particle class is characterized by a different sinking velocity: 0.025, <sup>c1</sup>1,  
 302 and 5 m/day. <sup>c2</sup>In this study, these particle classes are referred to as slow-, intermediate-,  
 303 and fast-sinking particles. This characterization is not based on the absolute  
 304 value of the sinking rate, but rather on the ratio with vertical currents in the study  
 305 region. The slowest-sinking class is essentially selected to represent non-sinking parti-  
 306 cles: based on the setup of our experiments, the slowest-sinking particles would take  
 307 400 days to sink 10 m through gravitational sinking, a timescale much greater than  
 308 commonly observed remineralization timescales. <sup>c3</sup>While 5 m/day remains a relatively  
 309 slow sinking rate, this “fastest-sinking” velocity is chosen as an end-member velocity  
 310 class of particle<sup>c4</sup>, based on the PDF of vertical velocities in the model. At any given  
 311 time, at least 85% of the model vertical velocity is weaker than 5 m/day. The results  
 312 presented for the 5 m/day sinking class can therefore be theoretically extrapolated to  
 313 any class with a higher sinking velocity.

314 The advective timestep for particles is set to 1.5 hours. The flow field is linearly  
 315 interpolated in time between model outputs, justifying the higher temporal resolution  
 316 used for particle tracking in *Papa\_winter*. Particle positions are saved every 3 hours,  
 317 along with key model variables interpolated onto the particle positions (e.g., density,  
 318 vorticity). Particles are tracked for <sup>c5</sup>four weeks (28 days). Each particle-tracking ex-  
 319 periment contains 1,971,717 particles per sinking-velocity class, for a total of 9,858,585  
 320 particles. Particles located deeper than the maximum winter mixed layer (i.e., 100 m;  
 321 Pelland et al., 2016; Plant et al., 2016) are considered exported, as they will likely not  
 322 be re-entrained into the mixed layer.

### 323 2.2.3 Density and Biomass Spectra

324 <sup>c6</sup>To quantify vertical export fluxes, both the distribution of the number of par-  
 325 ticles and the associated biomass can be modeled based on two main variables: the  
 326 particles’ radii and the rate at which the number of particles changes with respect to  
 327 the size. The particle number is modeled using a power-law function as a function of  
 328 size that is driven by the parameter  $\xi$ . This slope  $\xi$  of the size spectrum of particles  
 329 (also known as the Junge slope; White et al., 2015) is the slope of the log-log curve of

<sup>c1</sup> *Text added.*

<sup>c2</sup> *Available*

<sup>c2</sup> <https://www.waterproperties.ca/linep/index.php>

<sup>c1</sup> ~~0.05,~~

<sup>c2</sup> *Text added.*

<sup>c3</sup> *Text added.*

<sup>c4</sup> ~~that will be exported in its entirety over the course of our experiment.~~

<sup>c5</sup> ~~three~~

<sup>c6</sup> *Text added.*

particle number  $N$  vs. particle radius  $r$ , where

$$N(r) = N_0 \left( \frac{r}{r_0} \right)^{-\xi}. \quad (4)$$

Here,  $N_0$  and  $r_0$  represent a reference particle number and radius, chosen arbitrarily. <sup>c1</sup>Typical values for  $\xi$  derived from both in-situ observations and satellite data have been reported to range from 3 to 6 (Kostadinov, Siegel, & Maritorena, 2009; White et al., 2015, Z. Xiaodong, personal communication). For small particles ( $<400 \mu\text{m}$ ) and relatively low temperature ( $<15^\circ\text{C}$ ), it has been shown that the relationship between particle radius  $r$  and sinking velocity  $w_s$  exhibits a range of variation and is difficult to determine empirically. Nevertheless, Stokes' law, where  $w_s \propto r^2$ , is often used as a lower-bound sinking velocity estimate (Bach et al., 2012).

Assuming a Stokes-like relationship, we can construct based on (4) a particle sinking velocity spectrum  $N(w_s)$ , as <sup>c2</sup>a function of the Junge slope  $\xi$ :

$$N(w_s) = N_0 \left( \frac{w_s}{w_{s_0}} \right)^{-\xi/2}, \quad (5)$$

where  $w_{s_0}$  is the sinking speed of particles with radius  $r_0$ . For a specific slope and sinking-velocity class, an equivalent number of particles per simulated particle can be computed using (5) (See Figure 4). For example, using the largest sinking velocity class as a reference (i.e.,  $w_{s_0} = 5 \text{ m/day}$  and  $N_0 = 1,971,717$ ), and a spectral slope  $\xi = 4$ , each simulated particle with a sinking velocity of  $0.025 \text{ m/day}$  in fact represents 40,000 particles (Figure 4).

The relative biomass of a particle in a specific sinking-velocity class,  $B_p(w_s)$  can be estimated if the biomass is assumed to scale with the particle's volume. The relative biomass of one particle in a sinking-velocity class  $w_s$  can therefore be computed as

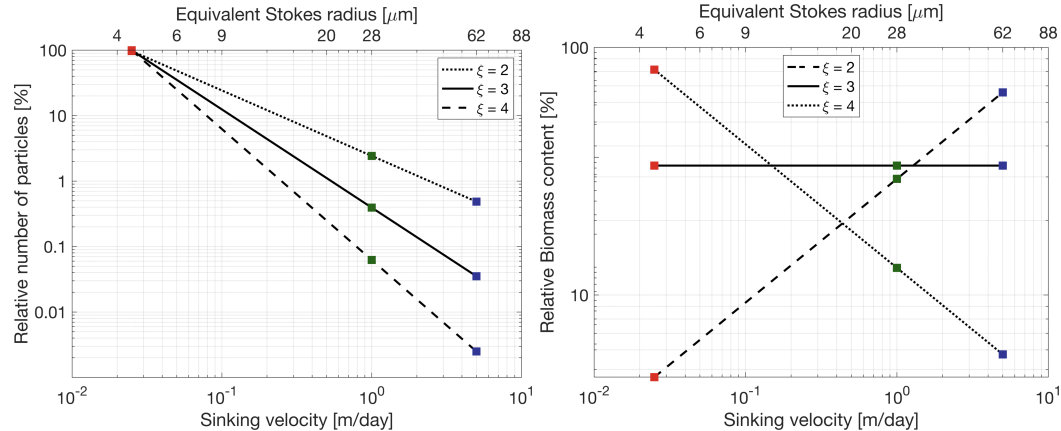


**Figure 4.** Relative number of particles (left) and biomass (right) as a function of sinking velocity  $w_s$ . Sinking velocity spectrum are shown for three different Junge slope  $\xi$ : 2 (dotted), 3 (solid), and 2 (dashed). Colored squares indicate the sinking velocities of the three particle classes modeled: 0.025 m/day (red), 1 m/day (green), and 5 m/day (blue).

<sup>c1</sup>Text added.

<sup>c2</sup>Text added.

$$B_p(w_s) = B_p(w_{s_0}) \left( \frac{w_s}{w_{s_0}} \right)^{3/2} \quad (6)$$

where  $B_p(w_{s_0})$  is the biomass of a particle in the sinking velocity class  $w_{s_0}$ . The total biomass associated with one simulated particle can be obtained by scaling (6) by the ratio  $N(w_s)/N_0$ :

$$B(w_s) = B_0 \left( \frac{w_s}{w_{s_0}} \right)^{3/2} \frac{N(w_s)}{N_0} \quad (7)$$

where  $B_0 = B_p(w_{s_0})$ . Combining (5) and (7) yields an expression relating the biomass associated with a simulated particle for a specific sinking-velocity class and the spectral slope (Figure 4):

$$B(w_s) = B_0 \left( \frac{w_s}{w_{s_0}} \right)^{\frac{3-\xi}{2}}. \quad (8)$$

Using the same example as before where  $\xi = 4$ , if the amount of biomass associated with one simulated particle in the 5 m/day sinking-velocity class is taken as  $B_0 = 1$ , then one simulated particle sinking at 0.025 m/day contains 14.14 units of biomass and a single particle contains  $14.14/40,000 = 3.5 \times 10^{-4}$  units of biomass (see Figure 4). This normalized formulation of particle number and biomass (see Equations (5) and (8)) has the advantage that the impact of spectral slope on the relative export of biomass can be quantified without needing a large number of particle-tracking experiments, where the number of seeded particles would vary to account for the different spectral slopes. For the purpose of this study, only the relative amount of biomass is relevant. For simplicity, we define a normalized biomass unit for  $\xi = 3$  as  $B_0 = 1$ . The values taken by  $B_0$  for other Junge slopes  $\xi$  are computed under the condition that the total amount of biomass is kept constant (Figure 4b).

#### 2.2.4 Particle Remineralization Scheme

Remineralization of particles as they sink through the water column impacts the amount of biomass exported. Slow-sinking particles generally contain less biomass and spend more time in the mixed layer, which means that they are remineralized at a shallower depth than faster sinking particles. Remineralization processes are complex, species-dependent, and generally not well-understood. In the absence of a consensus on a general functional form of particle remineralization, we rely on an idealized relationship which assumes that the biomass content of a particle decreases in time proportionally to the particle volume. Remineralization is thus modeled as an exponential decrease of biomass with time at a rate  $k$  (Iversen & Ploug, 2010, 2013)

$$B(t) = B^0 \exp(-kt), \quad (9)$$

where  $B^0$  denotes the biomass content at  $t = 0$  days, and the remineralization rate is taken to be  $k = 0.13 \text{ day}^{-1}$  in this study (Iversen & Ploug, 2010). This remineralization rate is independent of particle sinking velocity, and seems to lie within the range of other estimates (Iversen & Ploug, 2010, 2013; Ploug, Iversen, Koski, & Buitenhuis, 2008). The change in biomass with time is in turn expected to affect the sinking velocity of the particle. Given that  $B \propto w^{3/2}$  (see Equation (6)), particles in all sinking-velocity classes undergo a decay in sinking speed according to

$$w_s(t) = w_s^0 \exp\left(-\frac{2kt}{3}\right), \quad (10)$$

where  $w_s^0$  is the initial sinking velocity at  $t = 0$  days. In this study, the impact of remineralization is thus considered through the implementation of a time-dependent sinking velocity (Equation 10). While particles classes are classified based on their initial sinking-velocity, it is worth noting that over the length of the particle-tracking experiments that include remineralization (28 days), particle sinking speeds slow down to 10% of their initial velocity.

361 **3 Results**

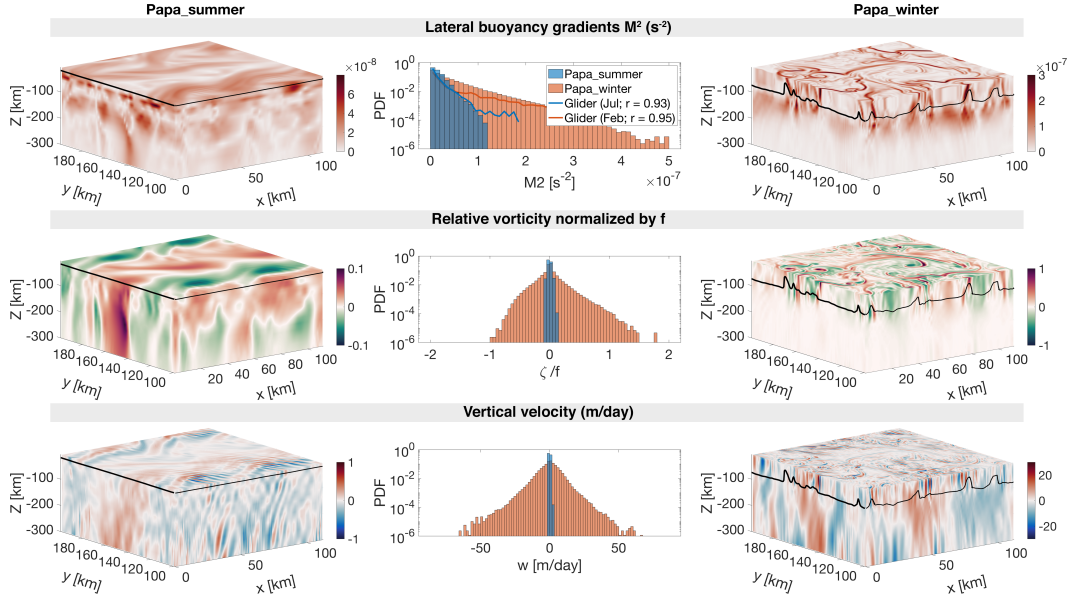
362 **3.1 Seasonally varying dynamical regimes**

363 Two model experiments are designed to capture different dynamical conditions  
 364 observed in the Northeast Pacific Ocean in summer and winter. *Papa\_summer* is ini-  
 365 tialized in early spring (doy 105) when the water column is characterized by a relatively  
 366 deep mixed layer ( $\sim 100$  m) and a halocline located between 100 and 150 m (Figure  
 367 2). The forcing by a realistic, positive, net heat flux generates the restratification of  
 368 the water column, with the development of a strong thermocline between 25 and 50 m  
 369 leading to the shoaling of the mixed layer and a subsurface peak in  $N^2$  at about 30 m  
 370 (see Figure 2). A comparison between model outputs and monthly-averaged density  
 371 profiles from underwater gliders collected in June and July over the period 2008-2009  
 372 yields correlation coefficients of  $r = 0.87$  and  $r = 0.88$ , respectively. These high cor-  
 373 relation suggest that *Papa\_summer* numerical experiment captures the vertical spring  
 374 and summer conditions in the Northeast Pacific Ocean.

375 In the horizontal, the prescribed density fronts progressively become unstable  
 376 within the first 60 days of the experiment (Figure 2). During this time, the Total  
 377 Kinetic Energy ( $KE_{tot}$ ) contained in the model domain slowly increases before reach-  
 378 ing a maximum at doy 162, where it remains relatively constant for the rest of the  
 379 simulation. The flattening of the  $KE_{tot}$  curve is used to determine the time necessary  
 380 for the simulation to spin-up, hence determining the start day of the particle-tracking  
 381 experiments. The ocean dynamics associated with *Papa\_summer* are characterized  
 382 using PDFs of horizontal buoyancy gradients ( $M^2 = |\nabla_H b|^2$ ), vertical velocities ( $w$ ),  
 383 and Rossby numbers computed from the normalized vertical component of the relative  
 384 vorticity ( $Ro = (v_x - u_y)/f$  where  $f = 1.12 \times 10^{-4}$ ; Figure 5).

392 Lateral buoyancy gradients in the summer are relatively weak  $\mathcal{O}(10^{-8} \text{ s}^{-2})$  and  
 393 result in low Rossby numbers  $\mathcal{O}(0.1)$ , with positive relative vorticity on the denser  
 394 (north) side of the front and negative relative vorticity on the lighter (south) side  
 395 of the front. Corresponding vertical velocities are consistently weaker than 1 m/day  
 396 ( $< 10^{-5} \text{ m/s}$ ) and are characterized by regions of weak upwelling and downwelling on  
 397 10 km scales, associated with the meandering of the front (Bower & Rossby, 1989).  
 398 Alternating bands of upwelling and downwelling at  $\mathcal{O}(1 \text{ km})$  spatial scale are super-  
 399 imposed, and likely caused by propagating internal waves. Coherent vertical velocities  
 400 structures extend to depths much greater than the mixed layer depth ( $\sim 25$  m; Figure  
 401 5). The amplitude of the vertical velocity field coincides with the expected order of  
 402 magnitude given by the scaling  $w \propto Ro f U / N$  (Mahadevan, 2016): using  $Ro \sim 0.1$   
 403 (Figure 5),  $N \sim 10^{-2} \text{ s}^{-1}$  (Figure 2),  $f \sim 10^{-5} \text{ s}^{-1}$ , and  $U \sim 0.01 \text{ m/s}$ , we obtain  
 404  $w \sim 10^{-6} \text{ m/s}$ , or  $\sim 10^{-1} \text{ m/day}$ .

405 *Papa\_winter* is, on the other hand, initialized in the winter (doy 0) to capture a  
 406 time period where the mixed layer depth is deeper ( $\sim 100$  m) and density gradients  
 407 more pronounced (Pelland et al., 2016). At this time of year, the water column in  
 408 this region is characterized by the presence of a deep halocline between 100 and 150  
 409 m (Figure 3 Pelland et al., 2016). After spin-up, the vertical stratification remains  
 410 consistent throughout the model run, and compares well with the vertical profile ob-  
 411 tained from glider observations for the month of March ( $r = 0.95$ ; see Figure 3). In  
 412 the horizontal, prescribed density fronts are much sharper than in summer (i.e., over  
 413 smaller spatial scales  $\mathcal{O}(1 \text{ km})$  vs.  $\mathcal{O}(10 \text{ km})$ ). Because of these stronger density  
 414 gradients, combined with the alternating zonal winds and constantly negative surface  
 415 heat flux, the fronts become unstable more rapidly than in summer (Figure 3). As a  
 416 result,  $KE_{tot}$  starts to plateau at doy 48. The experiment is considered spun-up by  
 417 doy 50 and the particle-tracking experiment is initialized.



385 **Figure 5.** Snapshots of  $M^2$  (top),  $\zeta/f$  (middle), and  $w$  (bottom) half-way through the  
 386 particle tracking experiment for *Papa\_summer* (left) and *Papa\_winter* (right), with the Mixed Layer  
 387 Depth indicated by the solid black line. The corresponding Probability Distribution Functions  
 388 (PDFs) are shown in the center for both *Papa\_summer* (blue) and *Papa\_winter* (red). Note the  
 389 different colorbars used for *Papa\_summer* and *Papa\_winter*. Histograms of  $M^2$  computed from  
 390 glider data at Station Papa in February (blue line) and July (red line) are superimposed in the  
 391 top middle panel.

418 The frontal structures visible in the horizontal buoyancy gradient field are as-  
 419 sociated with filaments of relatively high Rossby number of  $\mathcal{O}(1)$  (Figure 5). The  
 420 PDF of relative vorticity reveals a positively-skewed distribution ( $s = 0.68$ ). This is in  
 421 agreement with the fact that the relative vorticity is more likely to be cyclonic than an-  
 422 ticyclonic, based on conservation of potential vorticity (Hoskins & Bretherton, 1972).  
 423 Regions with high Rossby number are localized and located in the mixed layer exclu-  
 424 sively. In places where the local Rossby number reaches  $\mathcal{O}(1)$ , geostrophic balance is  
 425 lost and a vertical secondary ageostrophic circulation begins to slump the isopycnals  
 426 and restore the flow to a more geostrophically-balanced flow. This ageostrophic sec-  
 427 ondary circulation therefore generates “hot spots” of higher vertical velocities. The  
 428 fine-scale structures in the vertical velocity field corresponding to  $\mathcal{O}(1)$  Rossby num-  
 429 bers can be seen in Figure 5, with local vertical velocities up to 60 m/day ( $\sim 7 \times 10^{-4}$   
 430 m/s). Contrary to the PDF of relative vorticity ( $s = -0.25$ ). This is in agreement with the theory:  
 431 In fact, positive relative vorticity is associated with the dense side of a density front,  
 432 where vertical velocities are negative (Mahadevan, 2016). Once again, the amplitude  
 433 of these vertical velocity hot spots is coherent with the scaling  $w \propto RofU/N$ : using  
 434  $Ro \sim 1$ ,  $N \sim 10^{-2}$  1/s,  $f \sim 10^{-5}$  1/s, and  $U \sim 0.1$  m/s, we obtain  $w \sim 10^{-4}$  m/s, or  
 435  $\sim 10^1$  m/day.

437 Comparing *Papa\_summer* and *Papa\_winter* highlights the different dynamical  
 438 regimes in the two experiments. In *Papa\_winter*, density fronts tend to be sharper,  
 439 meaning larger density gradients over shorter spatial scales. When computed at the  
 440 kilometer-scale, the PDF of horizontal buoyancy gradients in *Papa\_winter* exhibits a  
 441 longer tail than in *Papa\_summer* (Figure 5). When compared to observations, the

442 PDFs of  $M^2$  in *Papa-summer* and *Papa-winter* demonstrate a correlation with obser-  
443 vations of  $r = 0.93$  and  $r = 0.95$ , respectively.

444 The wider PDF of vertical velocities in *Papa-winter* shows advective velocities  
445 that match and exceed typical gravitational sinking velocities, particularly for smaller,  
446 and therefore slower-sinking, particulate organic material. The secondary ageostrophic  
447 circulation that develops at submeso-scales (i.e.,  $\text{Ro} \sim O(1)$ ) therefore generates an ex-  
448 port mechanism that directly competes with the traditional paradigm that relies on  
449 gravitational sinking leading the export of particulate matter in the ocean.

### 450 3.2 Gravitational and Advective Export of POC

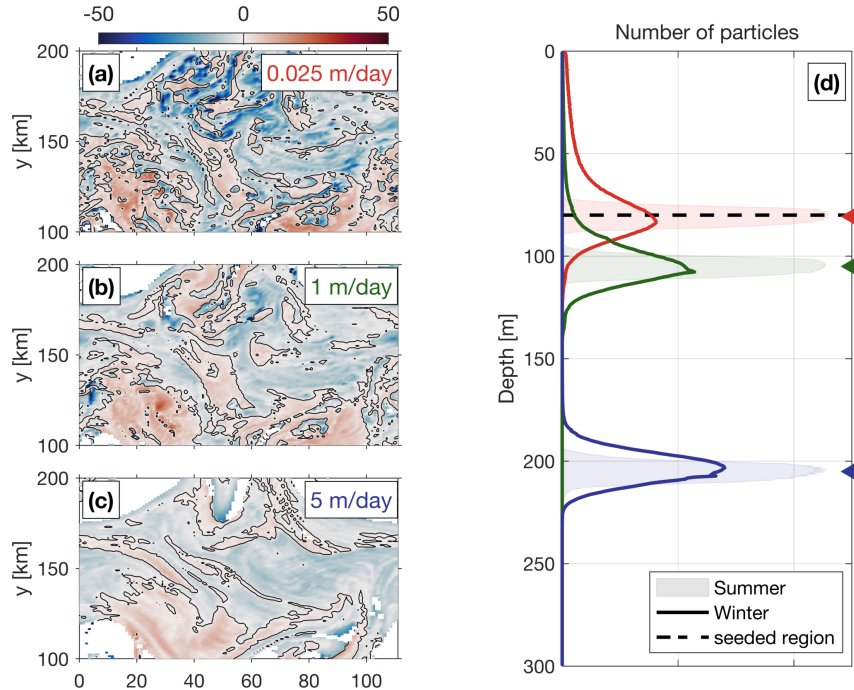
451 Both model experiments described above were then used to investigate the re-  
452 lationship between ocean dynamics and particle downward flux, using Lagrangian  
453 particle-tracking. Domain-averaged, downward particle flux is expected to be a com-  
454 bination of the flux driving by gravitational sinking ( $\langle w_s B \rangle$ ), and by the vertical ad-  
455 vective currents affecting the particle along its pathway ( $\langle wB \rangle$ ). The deviation in  
456 particle depths from the traditional one-dimensional gravitationally driven model is  
457 shown in Figure 6 for both summer and winter cases. In the summer, the PDF of par-  
458 ticle density versus depth remains relatively narrow through time, and is centered on  
459 a depth level that can be predicted using a simple 1D gravitational model (see shaded  
460 curves in Figure 6). The spread in the particle density also vary little among particle  
461 classes with different sinking velocities, suggesting that downward fluxes of particles  
462 is greatly dominated by gravitational settling and is not subject to significant vertical  
463 ocean currents.

475 In the winter, however, PDFs of particle density versus depth is wider, in agree-  
476 ment with the stronger vertical ocean currents occurring in the winter (see Figure 5).  
477 A top-view of the deviation in the downward particle flux from the traditionally con-  
478 sidered 1D gravitational model can be seen in Figure 6 (panels (a)-(c)). Slower-sinking  
479 particles deviate more than faster-sinking particles, exhibiting median depth anom-  
480 alies up to 50 m. This is due to the fact that slower-sinking particles spend more time  
481 in the mixed layer, where most of the stronger vertical currents tend to occur (Figure  
482 5). An interesting result emerges from the spatial distribution of the depth-anomaly:  
483 both positive (i.e., particles are shallower than expected) and negative (i.e., particles  
484 are deeper than expected) anomalies are organized into features with a length-scale  
485  $O(1\text{-}10 \text{ km})$ . This further highlights the importance of winter submesoscale circulation  
486 for vertical fluxes of particles.

487 A relative amount of biomass is associated to the particles using Equation (8).  
488 PDFs of relative biomass as a function of the vertical velocity is shown in Figure 7.  
489 Following the traditional paradigm derived from the simple 1D gravitational model, the  
490 downward flux of biomass in the summer is dominated by faster-sinking particle classes  
491 capable of carrying particulate material downwards more efficiently. The contribution  
492 of slower-sinking particles, however, depends critically on the slope of the size spectrum  
493 (see Figure 4). As the Junge slope increases, the spectrum of biomass steepens, and  
494 the relative contribution of slower-sinking particles to the downward biomass flux  
495 significantly increases (Figure 7c). In fact, the contribution of slower-sinking particles  
496 to the summer downward flux increases by a factor 100 (from 0.2% to  $c30\%$ ) when the  
497 Junge slope varies from  $\xi = 2$  to  $\xi = 4$ . While significant, the impact of a change in  
498 the Junge slope in summer conditions does not challenge the dominant role played by  
499 faster-sinking particles. This result can be explained by the fact that, in the summer,  
500 vertical velocities are weak and vertical biomass fluxes are therefore gravitationally-  
501 driven ( $\langle w_s B \rangle > \langle wB \rangle$ ).

---

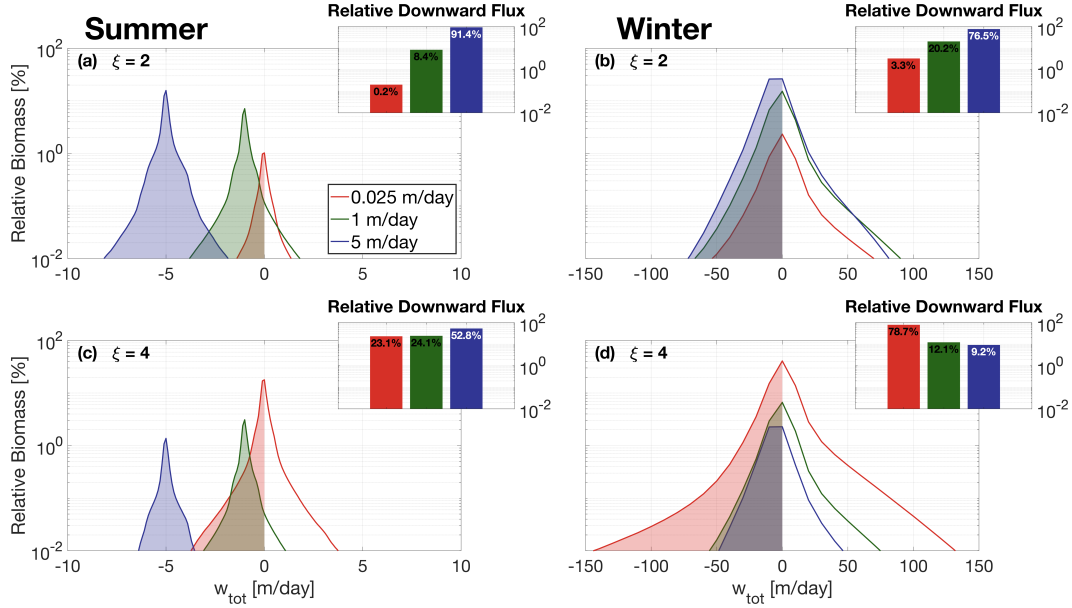
c3 2



464 **Figure 6.** [left] The median depth anomaly of particles with a sinking speed (a) 0.025 m/d,  
 465 (b) 1 m/d, (c) 5 m/d within each grid cell for the winter case 25 days after particles are released.  
 466 The ‘depth anomaly’ is with respect to the ‘expected’ sinking depth (= sinking speed  $\times$  time  
 467 since release). Blue (red) grid cells indicate that the median depth of particles in this cell is  
 468 deeper (shallower) than expected, based on a 1D gravitational model where  $z = w_s \times t$ . [right] (d)  
 469 Probability Distribution Function (PDF) of particles as a function of depth for each velocity class  
 470  $c^2$  (red = 0.025 m/day; green = 1 m/day; blue = 5 m/day). The winter distribution is shown as  
 471 thick lines, while the summer distribution is represented by the shaded regions. Triangle markers  
 472 indicate the expected depth of particles after 25 days based on the 1D gravitational model, which  
 473 is used as a reference to compute the depth anomalies. Release depth is indicated by the thick  
 474 dashed line.

509 In the winter, PDFs of relative biomass as a function of vertical velocities present  
 510 a much larger spread, with velocity magnitudes exceeding 50 m/day. For  $\xi = 2$ ,  
 511 the relative contribution of slower-sinking particles to the downward flux significantly  
 512 increases from 0.2% in the summer to about 3% in the winter, demonstrating the  
 513 impact advective velocities alone can have on vertical fluxes (Figure 7b). Nevertheless,  
 514 slower-sinking particles remain a relatively small contributor to the total downward  
 515 flux of biomass. When winter ocean dynamics are coupled with a steeper Junge slope,  
 516 however, slower-sinking particles largely dominate the downward biomass flux. In  
 517 our winter simulations with  $\xi = 4$ , we find that the slowest-sinking particle class is  
 518 responsible for about 79% of the biomass flux (Figure 7d).

519 Our results show that both a steepening of the particle size spectrum and the  
 520 presence of submesoscale dynamics can enhance the contribution of slower-sinking par-  
 521 ticles to the downward biomass flux. While the former is simply due to an increase in  
 522 particle density in slower-sinking particle classes, the latter is attributed to the larger  
 523 vertical velocity generated by submesoscale instabilities. When both are combined,  
 524 as expected in the wintertime, slower-sinking particles then become the leading con-  
 525 tributor to the downward biomass transport. However, slower-sinking particles are

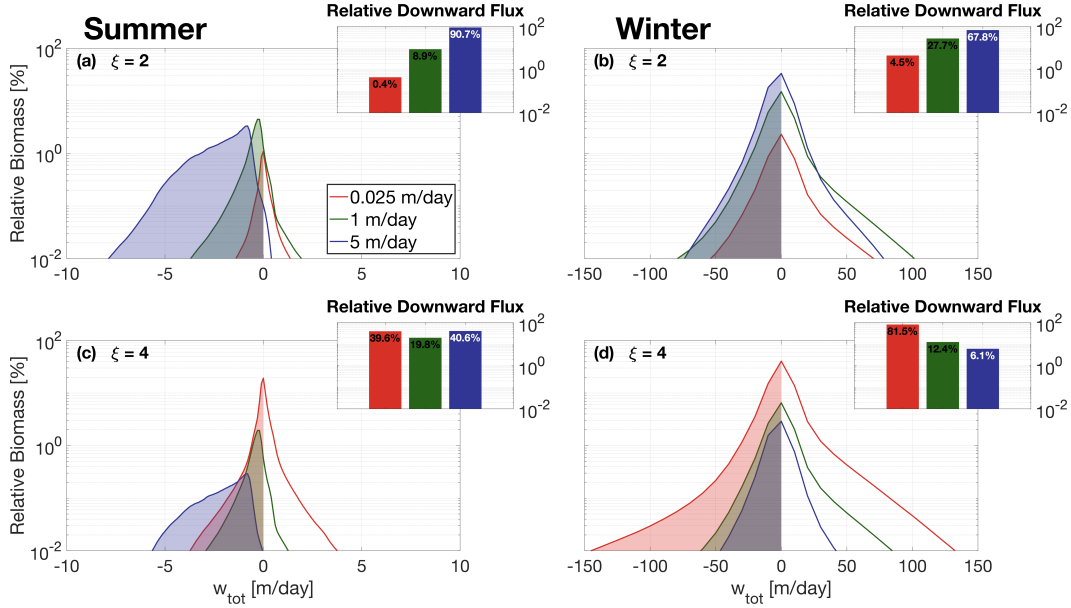


502 **Figure 7.** Probability Distribution Function (PDF) of relative biomass versus total vertical  
 503 velocity <sup>c7</sup>(sinking + advective) along particle trajectories in the summer case [left] and winter  
 504 case [right], with a Junge slope of 2 [top] and 4 [bottom]. <sup>c8</sup>PDFs are computed from the whole  
 505 24-day particle tracking experiments. Inserts show the integrated relative downward biomass flux  
 506 associated with each sinking-velocity class, categorized according to their initial sinking velocity  
 507 <sup>c9</sup>(red = 0.025 m/day; green = 1 m/day; blue = 5 m/day). Both winter dynamics and steeper  
 508 Junge slopes tend to increase the relative contribution of slower-sinking particles.

526 generally expected to remineralize on timescales shorter than their export timescale,  
 527 fueling the argument that the focus should be upon faster-sinking particle classes. The  
 528 impacts of remineralization on export are thus considered in the following section to  
 529 test the robustness of the findings.

### 530 3.3 Particle Remineralization

531 Both submesoscale dynamics and the Junge slope were identified as key factors  
 532 impacting the respective role played by different particle classes in driving downward  
 533 biomass fluxes. Simple Lagrangian particles were used to isolate the effects of these  
 534 two factors. In reality, however, sinking velocities of particulate matter varies in time  
 535 as the particles slowly remineralize. A remineralizing behavior was therefore imple-  
 536 mented for the Lagrangian particles, using Equation (10), to investigate the impact  
 537 that remineralization processes have on our findings. The traditional paradigm relies  
 538 on the fact that slow-sinking particles tend to fully remineralize over short timescales,  
 539 further enhancing the importance of faster-sinking particles classes in driving down-  
 540 ward biomass fluxes. While this paradigm holds for flatter Junge slope, where the  
 541 biomass content is dominated by faster-sinking particles, it becomes unfit at steeper  
 542 slopes.



555 **Figure 8.** <sup>c2</sup>Same as Figure 7, but including particle remineralization (see Equation 10).

543  
544 Figure 8 compares the relative biomass and downward biomass fluxes associated  
545 with each of the modeled particle classes for <sup>c1</sup> $\xi = 2$  and  $\xi = 4$  <sup>c2</sup>including  
546 the remineralization scheme. As previously detailed, downward fluxes of biomass  
547 are dominated by faster-sinking particles during summertime and in the absence of  
548 remineralization <sup>c3</sup>(see Figure 7). This is due to the fact that the flux of biomass  
549  $\langle w_{tot}B \rangle = \langle w_s B \rangle + \langle w B \rangle$  is driven by  $\langle w_s B \rangle$ , despite a smaller relative biomass content  
550 per particle. This is characteristic of a gravitationally-driven system, where settling  
551 velocity dictates the contribution to downward fluxes. Implementing remineralization  
552 processes, however, directly affects the particle settling velocity which slows down as  
553 particles remineralize. This effect can <sup>c4</sup>particularly be seen in Figure 8<sup>c5</sup>a and c,  
554 where PDFs of relative biomass per particle class are shifted towards weaker vertical  
555 velocities than in the absence of remineralization, as predicted by Equation (10). <sup>c6</sup>

556 In an advectively-driven system where  $\langle w_s B \rangle \sim \langle w B \rangle$ , the relative amount of  
557 biomass content in a particle class becomes important and dictates the respective con-  
558 tribution of each particle class to the total downward biomass fluxes. This shift from a  
559 gravitationally-driven to an advectively-driven system is observed when implementing  
560 particle remineralization in the summer (Figure 8<sup>c3</sup>): in the absence of remineral-  
561 ization, faster-sinking particles dominate the downward biomass fluxes (<sup>c4</sup>53%; see  
562 Figure 7c). When remineralization processes are considered, slower-sinking particles  
563 <sup>c5</sup>contribute more to biomass fluxes (see inset in Figure 8c). As shown in Figure 7,

<sup>c1</sup> Text added.

<sup>c2</sup> with and without

<sup>c3</sup> Text added.

<sup>c4</sup> Text added.

<sup>c5</sup> Text added.

<sup>c6</sup> As a result, the gravitationally-driven term  $\langle w_s B \rangle$  decreases with time, and the downward flux of  
biomass becomes generally advectively-driven by day 25 (Figure 8).

<sup>c3</sup> e

<sup>c4</sup> 60

<sup>c5</sup> become the dominant contributor

564 downward biomass fluxes in the wintertime are generally advectively-driven, due to the  
 565 larger vertical velocities associated with wintertime ocean dynamics. Biomass fluxes  
 566 are dominated by the slower-sinking particles <sup>c6</sup>when  $\xi = 4$ , representing 79% of the  
 567 downward biomass flux (Figure 7d). Even after implementing the remineralization  
 568 scheme, slower-sinking particles remain the largest contributor to downward biomass  
 569 fluxes (82%; see Figure 8d).

570 These results highlight the importance in considering slower-sinking particle  
 571 classes when considering downward biomass fluxes. It also demonstrates that, con-  
 572 trarily to the traditional paradigm, remineralization processes enhance the role played  
 573 by slower-sinking particles in biomass fluxes, in cases where the biomass spectrum  
 574 slope is negative.

## 575 4 Discussion

### 576 4.1 Dynamical Regimes

577 *Papa-summer* and *Papa-winter* experiments were designed to statistically cap-  
 578 ture the ocean dynamics at Station Papa (145°W, 50°N) in the Northeast Pacific  
 579 Ocean. After spin-up, the model demonstrated similar distributions of both horizontal  
 580 ( $M^2$ ) and vertical ( $N^2$ ) density gradients to observational estimates from underwater  
 581 gliders (see Figures 2, 3, and 5). The two experiments, however, show significantly  
 582 different distributions of  $M^2$ , with the winter distribution exhibiting a longer tail, due  
 583 to sharper density gradients. The tail of the wintertime distribution is only partially  
 584 captured by the glider data, due to the fact that underwater gliders sampled gradients  
 585 at spatial scales of 10 km and greater, while the model has a horizontal resolution of  
 586 500 m, allowing sharper submesoscale fronts and filaments to be formed.

587 Studies investigating submesoscale dynamics traditionally focused on regions  
 588 where the presence of submesoscale fronts and filaments are established, such as west-  
 589 ern boundary currents with strong gradients (D'Asaro, Lee, Rainville, Harcourt, &  
 590 Thomas, 2011; Thomas, Tandon, & Mahadevan, 2013), or the edge of mesoscale fea-  
 591 tures (van Haren et al., 2006; Waite et al., 2016). The seasonality in submesoscale  
 592 dynamics captured in the glider dataset at Station Papa and reflected in the model  
 593 experiments, echoes the behavior seen from recent observational studies conducted  
 594 at a similar latitude in the Atlantic Ocean, which demonstrate the intensification of  
 595 submesoscale dynamics in the wintertime (Buckingham et al., 2016; Thompson et al.,  
 596 2016). Despite being sometimes qualified as an “eddy desert” with low kinetic energy  
 597 (Chelton, Schlax, & Samelson, 2011), ocean characteristics in the eastern part of the  
 598 Pacific subpolar gyre suggest the presence of submesoscale features in the wintertime:  
 599 strong density gradients, localized Rossby numbers of order 1, a balanced Richardson  
 600 number  $Rib = \frac{f^2 N^2}{M^4}$  smaller than 1, a positively skewed distribution in vorticity, and a  
 601 negatively skewed distribution of vertical velocities (see Figure 5; Buckingham et al.,  
 602 2016; Rudnick, 2001; Thomas, Taylor, et al., 2013).

603 Strong downward velocities are hypothesized to enhance POC export by advect-  
 604 ing slower-sinking particles out of the mixed layer. *Papa-winter* indeed exhibits vertical  
 605 velocities more than 20 times larger than in *Papa-summer*. The vertical currents in  
 606 *Papa-winter*, however, tend to be much patchier than the weaker vertical currents  
 607 observed in *Papa-summer*. Because both particle production and downward vertical  
 608 velocities present a high degree of patchiness, it requires a certain level of covariance  
 609 between the two fields for the export to effectively be enhanced (Mahadevan et al.,  
 610 2012). A more realistic seeding strategy for Lagrangian particles, such as one guided

---

<sup>c6</sup> *Text added.*

611 by biological tracers, would likely provide important information towards a better  
 612 understanding of the effects of patchiness on POC export at submeso-scales

613 The hypothesis tested in this study is that submesoscale activity enhances export  
 614 of particulate matter at Station Papa by shortening the export timescale of particulate  
 615 matter. The wintertime intensification in submesoscale activity has the potential to  
 616 indeed enhance export (see discussion in Section 4.2). However, the seasonal cycle  
 617 in submesoscale activity is out of phase with the one in net community productivity,  
 618 which peaks in the spring and summertime when the mixed layer is shallower (Plant  
 619 et al., 2016). Two mechanisms are therefore present to potentially sustain a year-long  
 620 POC export flux: In the winter, less particulate material is present in the mixed layer,  
 621 but active submesoscale dynamics tend to enhance the POC export flux by advecting  
 622 the more numerous slower-sinking particles into the ocean interior. In the summer,  
 623 the production of POC is at its yearly maximum, but export tends to be dominated  
 624 by gravitational sinking, which favors faster-sinking particles and thus exclude part of  
 625 the particle spectrum from contributing to the export flux.

## 626 4.2 Downward Fluxes

627 Analyses of particle tracking experiments reveal that the contribution of slower-  
 628 sinking particles to the downward particulate flux depends on two main factors: (1)  
 629 the dynamics of the oceanic flow field, and (2) the slope of the size spectrum (i.e., the  
 630 Junge slope  $\xi$ ).

631 Mixed layer ocean dynamics at station Papa change significantly between the  
 632 winter and the summer. In the winter, submesoscale dynamics are intensified, and  
 633 sharp fronts and filaments develop in the mixed layer. This seasonal change in dy-  
 634 namics is consistent with recent observations (Buckingham et al., 2016; Thompson  
 635 et al., 2016), and models (Brannigan, Marshall, Naveira-Garabato, & George Nurser,  
 636 2015; Callies et al., 2015; Rocha, Gille, Chereskin, & Menemenlis, 2016) characterizing  
 637 the seasonal cycle of submesoscale dynamics. The winter intensification in subme-  
 638 soscale dynamics was proven to have an important impact on the downward flux of all  
 639 sinking-velocity classes modeled in this experiment.

640 In the summer, gravitational sinking governs a downward particulate flux, which  
 641 is dominated by faster-sinking particles, with little to no contribution from slower-  
 642 sinking particles. In the winter, however, vertical fluxes tend to be advectively-driven,  
 643 which leads to a slightly weaker downward flux of faster-sinking particles than in the  
 644 summer due to resuspension, but a much larger flux of slower-sinking particles, which  
 645 are present in far greater numbers (Figure 7). The gravitationally-driven flux in the  
 646 summer is mechanistically different from the advectively-driven winter flux, which  
 647 raises the question as to which process is most efficient in driving a downward flux of  
 648 particulate material.

649 In the absence of remineralization, both a steeper size spectrum slope ( $\xi > 3$  in  
 650 this case) and enhanced submesoscale dynamics, increase the contribution of slower-  
 651 sinking particle classes to the downward biomass flux. This is only when both of  
 652 these conditions are combined, however, that slower-sinking particles dominate the  
 653 downward flux of biomass (Figure 7). This is a significant result, as Junge slopes  
 654 greater than 3 have been observed in the ocean <sup>c1</sup>: In-situ observations yield aver-  
 655 age spectral slopes varying between 3.5 and 4.5 (Kostadinov et al., 2009, see Table 2  
 656 in )<sup>c2</sup>, while spectral analysis of satellite data suggest global spectral slopes varying  
 657 between 3 and 6. More recent observational work located in the Northeast Pacific,

---

<sup>c1</sup> *Text added.*

<sup>c2</sup> *Text added.*

including Station Papa, found a spectral slope also greater than 3 (White et al., 2015; ; Z. Xiaodong, personal communication). <sup>c3</sup> Junge slopes are expected to vary in space, depending on the community composition, both lateraly and vertically (Kostadinov et al., 2009; White et al., 2015)<sup>c4</sup>, as well as in time; spectrum slopes tend to be flatter during a spring bloom event, where larger particles (e.g., diatoms) are produced in large quantities, and steeper during the wintertime, when communities are mostly composed of small particles (Behrenfeld, 2010; Dale, Rey, & Heimdal, 1999; Parsons & Lalli, 1988). The threshold value of  $\xi = 3$  for a change in the biomass spectral slope (see Figure 4b) is of course a consequence of first-order approximations used in this study describing the relationships between particle size, sinking velocity, and biomass content. Nevertheless, our results demonstrate the importance of including the smaller particle size range of the particle spectrum, in the estimation or measurement of vertical fluxes, especially when submesoscale dynamics are active. It also highlights the importance of better constraining the relationships linking particle size, sinking velocity, and biomass content.

Introducing remineralization processes significantly decreases the biomass flux. Counter-intuitively, however, the implementation of a remineralization scheme further strengthens the contribution of slower-sinking particles to the biomass flux (Figure 8). This can be explained by the fact that remineralization processes have a greater impact on sinking-velocity classes that rely on gravitational sinking to be exported, as these particles decelerate as they remineralize. In the summer, all particle classes are similarly affected by remineralization, as downward fluxes are gravitationally-driven. In the winter, however, slower-sinking particles are exported through advective processes. Their export timescale is barely affected by remineralization processes as it only depends on local ocean dynamics.

<sup>c1</sup> These results are robust to the range of sinking rates explored. If one considers a particle class with a sinking rate far exceeding the vertical advective velocity (e.g., 100 m/day; Turner, 2015)<sup>c2</sup>, then the associated biomass flux can be estimated by relying on the traditional 1-D paradigm, assuming  $w_{tot} \approx w_s$ . Combining this approximation with Equation 8 shows that the slope of the biomass flux spectrum is positive for  $\xi < 5$ , in which case very fast-sinking particles would dominate vertical biomass fluxes. However, for  $\xi > 5$ , the slope of the biomass flux spectrum becomes negative as well, meaning that the biomass flux is always dominated by the slow-sinking particle classes, regardless of the ocean dynamical regime. While considered large, values of  $\xi > 5$  remain realistic and fall within the range obtained from satellite-based estimates (Kostadinov et al., 2009).

The results of this study suggest that slow- and non-sinking particles must be considered when studying the downward flux of particulate matter in the upper ocean. The patchiness associated with both particle production and submesoscale features poses a real observational challenge to properly resolve vertical fluxes. Based on our findings, subsequent studies should focus on testing the impact of patchiness on vertical fluxes. In the wintertime, when size spectral slope is steep and submesoscale dynamics most active, vertical fluxes could be grossly underestimated depending on the level of co-occurrence between particle production and stronger vertical currents.

## 5 Conclusion

The main conclusions of this study are:

---

<sup>c3</sup> Text added.

<sup>c4</sup> Text added.

<sup>c1</sup> Text added.

<sup>c2</sup> Text added.

- 704 1. Ocean dynamics in the subpolar Northeast Pacific exhibit a seasonal cycle with  
 705 low submesoscale activity in the summertime, and more submesoscale features  
 706 present in the wintertime. Submesoscale dynamics generate larger, and asym-  
 707 metric, vertical currents leading to a vertical biomass flux driven by advective  
 708 processes, as opposed to gravitational sinking in the summertime.
- 709 2. Submesoscale dynamics generally enhance the downward particulate flux by  
 710 increasing the contribution of slower-sinking particles to the total flux through  
 711 advective transport. The slower-sinking particles are found to be significant  
 712 for export, and can be even make the dominant contribution under certain  
 713 conditions.
- 714 3. The contribution of slower-sinking particles to the downward biomass flux de-  
 715 pends on the slope of the particle size spectra (i.e., the Junge Slope), that  
 716 controls the relative number of particles per size class. Two cases emerge from  
 717 this study:
- 718 (a) If the Junge slope is smaller than 3, larger particles contribute most to vertical  
 719 biomass fluxes independently of flow dynamics, as there are no mechanisms  
 720 capable of selectively advecting slower-sinking particles. The system is de-  
 721 scribed as gravitationally-driven.
- 722 (b) If the Junge slope is greater than 3, as most commonly observed, ocean  
 723 dynamics become key for determining which particle classes dominate the  
 724 downward flux. As submesoscale dynamics become more active, ageostrophic  
 725 circulations leading to larger vertical velocities develop. In these conditions,  
 726 downward biomass fluxes are largely driven by the slower-sinking particle  
 727 classes.
- 728 4. Remineralization processes logically reduce the amount of biomass flux. How-  
 729 ever, it unexpectedly enhances the role of slower-sinking particles, which are are  
 730 advectively transported. The impact of remineralization is greater on faster-  
 731 sinking particles since it affects both the biomass content and their sinking  
 732 velocity.

### 733 Acknowledgments

734 The work was funded by NASA grant NNX16AR48G, to complement the EXport  
 735 Processes in the global Ocean from RemoTe Sensing (EXPORTS) program. We would  
 736 like to thank A. Thompson (Caltech) for his useful comments and suggestions, N.  
 737 Pelland (NOAA) and C. Eriksen (University of Washington) for sharing the glider data  
 738 collected at Ocean Station Papa, as well as S. Essink for his assistance in developing the  
 739 particle-tracking code. All data used in this manuscript are publicly available: Ocean  
 740 Station Papa data is available on PMEL's website (<https://www.pmel.noaa.gov/ocs/Papa>; PMEL, 2018) and gridded Argo products can be downloaded at <http://www.seanoe.org/data/00348/45945> (Gaillard, 2015). Glider data is archived at the  
 741 University of Washington's Library (<http://hdl.handle.net/1773/41656>; Pelland,  
 742 2018). Code to reproduce analysis and figures are publicly available at [https://github.com/matdever/Size-differentiated\\_Export\\_GBC](https://github.com/matdever/Size-differentiated_Export_GBC) (Dever, 2020). Due to the  
 743 very large filesize, model outputs and particle trajectories are available on request.  
 744

### 747 References

- 748 Alkire, M., D'Asaro, E., Lee, C., Perry, M., Gray, A., Cetinic, I., ... González-  
 749 Posada, A. (2012). Estimates of net community production and export using  
 750 high-resolution, Lagrangian measurements of O<sub>2</sub>, NO<sub>3</sub><sup>-</sup>, and POC through the  
 751 evolution of a spring diatom bloom in the North Atlantic. *Deep-Sea Res. I*,  
 752 64, 157-174. doi: 10.1016/j.dsr.2012.01.012

- 753 Armstrong, R. A., Lee, C., Hedges, J. I., Honjo, S., & Wakeham, S. G. (2001). A  
 754 new, mechanistic model for organic carbon fluxes in the ocean based on the  
 755 quantitative association of POC with ballast minerals. *Deep Sea Research Part*  
 756 *II*, 49(1), 219–236. doi: 10.1016/S0967-0645(01)00101-1
- 757 Bach, L. T., Riebesell, U., Sett, S., Febiri, S., Rzepka, P., & Schulz, K. G. (2012).  
 758 An approach for particle sinking velocity measurements in the 3–400  $\mu\text{m}$  size  
 759 range and considerations on the effect of temperature on sinking rates. *Marine*  
 760 *Biology*, 159(8), 1853–1864. doi: 10.1007/s00227-012-1945-2
- 761 Baker, C. A., Henson, S. A., Cavan, E. L., Giering, S. L., Yool, A., Gehlen, M., ...  
 762 Sanders, R. (2017). Slow-sinking particulate organic carbon in the atlantic  
 763 ocean: Magnitude, flux, and potential controls. *Global Biogeochemical Cycles*,  
 764 31(7), 1051–1065. doi: 10.1002/2017GB005638
- 765 Behrenfeld, M. J. (2010). Abandoning sverdrup's critical depth hypothesis on phyto-  
 766 plankton blooms. *Ecology*, 91(4), 977–989. doi: 10.1890/09-1207.1
- 767 Bower, A. S., & Rossby, T. (1989). Evidence of Cross-Frontal Exchange Processes  
 768 in the Gulf Stream Based on Isopycnal RAFOS Float Data. *Journal of Phys-*  
 769 *ical Oceanography*, 19(9), 1177–1190. doi: 10.1175/1520-0485(1989)019<1177:  
 770 EOCFEP>2.0.CO;2
- 771 Brannigan, L., Marshall, D. P., Naveira-Garabato, A., & George Nurser, A. (2015).  
 772 The seasonal cycle of submesoscale flows. *Ocean Modelling*, 92, 69–84. doi: 10  
 773 .1016/j.ocemod.2015.05.002
- 774 Briggs, N., Perry, M. J., Cetinić, I., Lee, C., D'Asaro, E., Gray, A. M., & Rehm, E.  
 775 (2011). High-resolution observations of aggregate flux during a sub-polar north  
 776 atlantic spring bloom. *Deep Sea Research Part I: Oceanographic Research*  
 777 *Papers*, 58(10), 1031 – 1039. doi: 10.1016/j.dsr.2011.07.007
- 778 Buckingham, C. E., Naveira Garabato, A. C., Thompson, A. F., Brannigan, L.,  
 779 Lazar, A., Marshall, D. P., ... Belcher, S. E. (2016). Seasonality of sub-  
 780 mesoscale flows in the ocean surface boundary layer. *Geophysical Research*  
 781 *Letters*, 43(5), 2118–2126. doi: 10.1002/2016GL068009
- 782 Callies, J., Ferrari, R., Klymak, J. M., & Gula, J. (2015). Seasonality in sub-  
 783 mesoscale turbulence. *Nature communications*, 6, 6862. doi: 10.1038/  
 784 ncomms7862
- 785 Chelton, D. B., Schlax, M. G., & Samelson, R. M. (2011). Global observations of  
 786 nonlinear mesoscale eddies. *Progress in Oceanography*, 91(2), 167–216. doi: 10  
 787 .1016/j.pocean.2011.01.002
- 788 Dale, T., Rey, F., & Heimdal, B. R. (1999). Seasonal development of phytoplankton  
 789 at a high latitude oceanic site. *Sarsia*, 84(5-6), 419–435. doi: 10.1080/00364827  
 790 .1999.10807347
- 791 D'Asaro, E., Lee, C., Rainville, L., Harcourt, R., & Thomas, L. (2011). Enhanced  
 792 turbulence and energy dissipation at ocean fronts. *Science*, 332(6027), 318–  
 793 322. doi: 10.1126/science.1201515
- 794 Dever, M. (2020). *Size differentiated Export GBC: Release 1*. (data retrived from  
 795 GitHub, [https://github.com/matdever/Size-differentiated\\_Export\\_GBC](https://github.com/matdever/Size-differentiated_Export_GBC))  
 796 doi: 10.5281/zenodo.3908126
- 797 DeVries, T., Liang, J.-H., & Deutsch, C. (2014). A mechanistic particle flux model  
 798 applied to the oceanic phosphorus cycle. *Biogeosciences*, 11(19), 5381–5398.  
 799 doi: 10.5194/bg-11-5381-2014
- 800 Döös, K., Kjellsson, J., & Jönsson, B. (2013). TRACMASS – A Lagrangian Trajec-  
 801 tory Model. In *Preventive methods for coastal protection* (pp. 225–249). Heidel-  
 802 berg: Springer International Publishing. doi: 10.1007/978-3-319-00440-2\_7
- 803 Ducklow, H. W., Steinberg, D. K., & Buesseler, K. O. (2001). Upper Ocean Carbon  
 804 Export and the Biological Pump. *Oceanography*, 14. doi: <https://doi.org/10.5670/oceanog.2001.06>
- 805 Estapa, M. L., Siegel, D. A., Buesseler, K. O., Stanley, R. H. R., Lomas, M. W., &  
 806 Nelson, N. B. (2015). Decoupling of net community and export production

- 808       on submesoscales in the Sargasso Sea.     *Global Biogeochemical Cycles*, *29*(8),  
 809       1266–1282. doi: 10.1002/2014GB004913
- 810       Falkowski, P. G., Barber, R. T., & Smetacek, V. (1998). Biogeochemical Controls  
 811       and Feedbacks on Ocean Primary Production.     *Science*, *281*(5374), 200–206.  
 812       doi: 10.1126/science.281.5374.200
- 813       Fox-Kemper, B., Ferrari, R., & Hallberg, R. (2008). Parameterization of Mixed  
 814       Layer Eddies. Part I: Theory and Diagnosis.     *Journal of Physical Oceanogra-*  
 815       phy, *38*(6), 1145–1165. doi: 10.1175/2007JPO3792.1
- 816       Gaillard, F. (2015). *ISAS-13 temperature and salinity gridded fields. SEANOE*. doi:  
 817       10.17882/45945
- 818       Gaillard, F., Reynaud, T., Thierry, V., Kolodziejczyk, N., & von Schuckmann, K.  
 819       (2016). In situ-based reanalysis of the global ocean temperature and salinity  
 820       with isas: Variability of the heat content and steric height.     *Journal of Climate*,  
 821       *29*(4), 1305–1323. doi: 10.1175/JCLI-D-15-0028.1
- 822       Gruber, N., Lachkar, Z., Frenzel, H., Marchesiello, P., Münnich, M., McWilliams,  
 823       J. C., ... Plattner, G.-K. (2011). Eddy-induced reduction of biological pro-  
 824       duction in eastern boundary upwelling systems.     *Nature geoscience*, *4*(11), 787.  
 825       doi: 10.1038/NGEO1273
- 826       Harrison, P. J., Whitney, F. A., Tsuda, A., Saito, H., & Tadokoro, K. (2004).  
 827       Nutrient and Plankton Dynamics in the NE and NW Gyres of the Sub-  
 828       arctic Pacific Ocean.     *Journal of Oceanography*, *60*(1), 93–117.       doi:  
 829       10.1023/B:JOCE.0000038321.57391.2a
- 830       Hoskins, B. J., & Bretherton, F. P. (1972). Atmospheric Frontogenesis Models:  
 831       Mathematical Formulation and Solution.     *Journal of the Atmospheric Sciences*,  
 832       *29*(1), 11–37. doi: 10.1175/1520-0469(1972)029<0011:AFMMFA>2.0.CO;2
- 833       Iversen, M. H., & Ploug, H. (2010). Ballast minerals and the sinking carbon flux in  
 834       the ocean: carbon-specific respiration rates and sinking velocity of marine snow  
 835       aggregates.     *Biogeosciences*, *7*(9), 2613–2624. doi: 10.5194/bg-7-2613-2010
- 836       Iversen, M. H., & Ploug, H. (2013). Temperature effects on carbon-specific respi-  
 837       ration rate and sinking velocity of diatom aggregates - potential implications  
 838       for deep ocean export processes.     *Biogeosciences*, *10*(6), 4073–4085.       doi:  
 839       10.5194/bg-10-4073-2013
- 840       Jackson, G. A., Maffione, R., Costello, D. K., Alldredge, A. L., Logan, B. E., &  
 841       Dam, H. G. (1997). Particle size spectra between 1  $\mu\text{m}$  and 1 cm at Monterey  
 842       Bay determined using multiple instruments.     *Deep Sea Research Part I*, *44*(11),  
 843       1739–1767. doi: 10.1016/S0967-0637(97)00029-0
- 844       Klein, P., & Lapeyre, G. (2009). The Oceanic Vertical Pump Induced by Mesoscale  
 845       and Submesoscale Turbulence.     *Annual Review of Marine Science*, *1*(1), 351–  
 846       375. doi: 10.1146/annurev.marine.010908.163704
- 847       Kostadinov, T. S., Siegel, D. A., & Maritorena, S. (2009). Retrieval of the particle  
 848       size distribution from satellite ocean color observations.     *Journal of Geophysical*  
 849       *Research*, *114*(C9), C09015. doi: 10.1029/2009JC005303
- 850       Lévy, M., Ferrari, R., Franks, P. J. S., Martin, A. P., & Rivière, P. (2012). Bringing  
 851       physics to life at the submesoscale.     *Geophysical Research Letters*, *39*(14), n/a–  
 852       n/a. doi: 10.1029/2012GL052756
- 853       Lévy, M., Klein, P., & Treguier, A.-M. (2001). Impact of sub-mesoscale physics on  
 854       production and subduction of phytoplankton in an oligotrophic regime.     *Jour-*  
 855       *nal of marine research*, *59*(4), 535–565. doi: 10.1357/002224001762842181
- 856       Mahadevan, A. (2016). The Impact of Submesoscale Physics on Primary Produc-  
 857       tivity of Plankton.     *Annual Review of Marine Science*, *8*(1), 161–184. doi: 10  
 858       .1146/annurev-marine-010814-015912
- 859       Mahadevan, A., & Archer, D. (2000). Modeling the impact of fronts and  
 860       mesoscale circulation on the nutrient supply and biogeochemistry of the up-  
 861       per ocean.     *Journal of Geophysical Research: Oceans*, *105*(C1), 1209–1225. doi:  
 862       10.1029/1999JC900216

- 863 Mahadevan, A., D'Asaro, E., Lee, C., & Perry, M. J. (2012). Eddy-Driven Stratification Initiates North Atlantic Spring Phytoplankton Blooms. *Science*,  
864 337(6090), 54–58. doi: 10.1126/science.1218740
- 865 Mahadevan, A., Olinger, J., & Street, R. (1996a). A Nonhydrostatic Mesoscale Ocean  
866 Model. Part II: Numerical Implementation. *Journal of Physical Oceanography*,  
867 26(9), 1881–1900. doi: 10.1175/1520-0485(1996)026<1881:ANMOMP>2.0.CO;  
868 2
- 870 Mahadevan, A., Olinger, J., & Street, R. (1996b). A Nonhydrostatic mesoscale ocean  
871 model. Part I: Well-posedness and scaling. *Journal of Physical Oceanography*,  
872 26(9), 1868–1880. doi: 10.1175/1520-0485(1996)026<1868:ANMOMP>2.0.CO;  
873 2
- 874 Mahadevan, A., & Tandon, A. (2006). An analysis of mechanisms for submesoscale  
875 vertical motion at ocean fronts. *Ocean Modelling*, 14(3-4), 241–256. doi: 10  
876 .1016/J.OCEMOD.2006.05.006
- 877 McCave, I. (1984). Size spectra and aggregation of suspended particles in the deep  
878 ocean. *Deep Sea Research Part I*, 31(4), 329–352. doi: 10.1016/0198-0149(84)  
879 90088-8
- 880 McDonnell, A., & Buesseler, K. (2012). A new method for the estimation of sinking  
881 particle fluxes from measurements of the particle size distribution, average  
882 sinking velocity, and carbon content. *Limnology and Oceanography: Methods*,  
883 10, 329–346. doi: 10.4319/lom.2012.10.329
- 884 McDonnell, A. M. P., & Buesseler, K. O. (2010). Variability in the average sinking  
885 velocity of marine particles. *Limnology and Oceanography*, 55(5), 2085–2096.  
886 doi: 10.4319/lo.2010.55.5.2085
- 887 McWilliams, J. C. (2016). Submesoscale currents in the ocean. *Proceedings of the  
888 Royal Society A: Mathematical, Physical and Engineering Science*, 472(2189).  
889 doi: 10.1098/rspa.2016.0117
- 890 Mensa, J. A., Garraffo, Z., Griffa, A., Özgökmen, T. M., Haza, A., & Veneziani, M.  
891 (2013). Seasonality of the submesoscale dynamics in the Gulf Stream region.  
892 *Ocean Dynamics*, 63(8), 923–941. doi: 10.1007/s10236-013-0633-1
- 893 Mesinger, F., DiMego, G., Kalnay, E., Mitchell, K., Shafran, P. C., Ebisuzaki, W.,  
894 ... Shi, W. (2006). North american regional reanalysis. *Bulletin of the Ameri-  
895 can Meteorological Society*, 87(3), 343–360. doi: 10.1175/BAMS-87-3-343
- 896 Omand, M. M., D'Asaro, E. A., Lee, C. M., Perry, M. J., Briggs, N., Cetini, I.,  
897 & Mahadevan, A. (2015). Eddy-driven subduction exports particulate or-  
898 ganic carbon from the spring bloom. *Science*, 348(6231), 222–225. doi:  
899 10.1126/science.1260062
- 900 Omand, M. M., Govindarajan, R., He, J., & Mahadevan, A. (2020). Sinking flux of  
901 particulate organic matter in the oceans: Sensitivity to particle characteristics.  
902 *Scientific reports*, 10(1), 1–16. doi: 10.1038/s41598-020-60424-5
- 903 Parsons, T. R., & Lalli, C. M. (1988). Comparative oceanic ecology of the plankton  
904 communities of the subarctic Atlantic and Pacific oceans. *Oceanography and  
905 Marine Biology Annual Review*, 26, 317–359.
- 906 Pelland, N. (2018). *Seaglider Surveys at Ocean Station Papa: Bin-Averaged Profiles,  
907 Currents, and Independent Oxygen Data*. Retrieved from <http://hdl.handle.net/1773/41656>
- 908 Pelland, N., Eriksen, C., & Cronin, M. (2016). Seaglider surveys at Ocean Station  
909 Papa: Circulation and watermass properties in a meander of the North Pa-  
910 cific Current. *Journal of Geophysical Research: Oceans*, 121, 6816–6846. doi:  
911 10.1002/2016JC011920
- 912 Petrik, C., Jackson, G., & Checkley, D. (2013). Aggregates and their distributions  
913 determined from LOPC observations made using an autonomous profiling  
914 float. *Deep Sea Research Part I*, 74, 64–81. doi: 10.1016/j.dsr.2012.12.009
- 915 Plant, J. N., Johnson, K. S., Sakamoto, C. M., Jannasch, H. W., Coletti, L. J.,  
916 Riser, S. C., & Swift, D. D. (2016). Net community production at Ocean Sta-

- tion Papa observed with nitrate and oxygen sensors on profiling floats. *Global Biogeochemical Cycles*, 30(6), 859–879. doi: 10.1002/2015GB005349
- Ploug, H., Iversen, M. H., Koski, M., & Buitenhuis, E. T. (2008). Production, oxygen respiration rates, and sinking velocity of copepod fecal pellets: Direct measurements of ballasting by opal and calcite. *Limnology and Oceanography*, 53(2), 469–476. doi: 10.4319/lo.2008.53.2.0469
- PMEL. (2018). *Pacific Marine Environment Laboratory Ocean Climate Stations Mooring Data*. Retrieved from <https://www.pmel.noaa.gov/ocs/data-overview>
- Richardson, T., & Jackson, G. (2007). Small phytoplankton and carbon export from the surface ocean. *Science*, 315, 838–840. doi: 10.1126/science.1133471
- Riley, J., Sanders, R., Marsay, C., Le Moigne, F. A., Achterberg, E. P., & Poulton, A. J. (2012). The relative contribution of fast and slow sinking particles to ocean carbon export. *Global Biogeochemical Cycles*, 26(1). doi: 10.1029/2011GB004085
- Rocha, C. B., Gillett, S. T., Chereskin, T. K., & Menemenlis, D. (2016). Seasonality of submesoscale dynamics in the Kuroshio Extension. *Geophysical Research Letters*, 43(21), 11,304–11,311. doi: 10.1002/2016GL071349
- Rudnick, D. L. (2001). On the skewness of vorticity in the upper ocean. *Geophysical Research Letters*, 28(10), 2045–2048. doi: 10.1029/2000GL012265
- Sheldon, R., Prakash, A., & Sutcliffe, W., Jr. (1972). The size distribution of particles in the ocean. *Limnology and Oceanography*, 17(3), 327–340. doi: 10.4319/lo.1972.17.3.0327
- Sherry, N. D., Boyd, P. W., Sugimoto, K., & Harrison, P. J. (1999). Seasonal and spatial patterns of heterotrophic bacterial production, respiration, and biomass in the subarctic NE Pacific. *Deep-Sea Research Part II: Topical Studies in Oceanography*, 46(11–12), 2557–2578. doi: 10.1016/S0967-0645(99)00076-4
- Stukel, M. R., Aluwihare, L. I., Barbeau, K. A., Chekalyuk, A. M., Goericke, R., Miller, A. J., ... others (2017). Mesoscale ocean fronts enhance carbon export due to gravitational sinking and subduction. *Proceedings of the National Academy of Sciences*, 114(6), 1252–1257. doi: 10.1073/pnas.1609435114
- Taylor, J. R., Smith, K. M., & Vreugdenhil, C. A. (2020). The influence of submesoscales and vertical mixing on the export of sinking tracers in large-eddy simulations. *Journal of Physical Oceanography*, 50(5), 1319–1339. doi: 10.1175/JPO-D-19-0267.1
- Thomas, L. N., Tandon, A., & Mahadevan, A. (2013). Submesoscale processes and dynamics. In *Ocean modeling in an eddying regime* (p. 17–38). American Geophysical Union (AGU). doi: 10.1029/177GM04
- Thomas, L. N., Taylor, J. R., Ferrari, R., & Joyce, T. M. (2013). Symmetric instability in the Gulf Stream. *Deep Sea Research Part II: Topical Studies in Oceanography*, 91, 96–110. doi: 10.1016/j.dsr2.2013.02.025
- Thompson, A. F., Lazar, A., Buckingham, C., Naveira Garabato, A. C., Damerell, G. M., & Heywood, K. J. (2016). Open-Ocean Submesoscale Motions: A Full Seasonal Cycle of Mixed Layer Instabilities from Gliders. *Journal of Physical Oceanography*, 46(4), 1285–1307. doi: 10.1175/JPO-D-15-0170.1
- Turner, J. T. (2015). Zooplankton fecal pellets, marine snow, phytodetritus and the ocean's biological pump. *Progress in Oceanography*, 130, 205–248.
- van Haren, H., Millot, C., & Taupier-Letage, I. (2006). Fast deep sinking in Mediterranean eddies. *Geophysical Research Letters*, 33(4), L04606. doi: 10.1029/2005GL025367
- Waite, A. M., Stemmann, L., Guidi, L., Calil, P. H. R., Hogg, A. M. C., Feng, M., ... Gorsky, G. (2016). The wineglass effect shapes particle export to the deep ocean in mesoscale eddies. *Geophysical Research Letters*, 43(18), 9791–9800. doi: 10.1002/2015GL066463
- White, A. E., Letelier, R. M., Whitmire, A. L., Barone, B., Bidigare, R. R., Church,

- 973 M. J., & Karl, D. M. (2015). Phenology of particle size distributions  
974 and primary productivity in the North Pacific subtropical gyre (Station  
975 ALOHA). *Journal of Geophysical Research: Oceans*, 120(11), 7381–7399.  
976 doi: 10.1002/2015JC010897